RSC Advances

PAPER

View Article Online
View Journal | View Issue

Cite this: *RSC Adv.*, 2025, **15**, 32732

Low-temperature phosphidation synthesis of flower-like Ru-CoVO-P polymetallic catalyst for enhanced overall water splitting in alkaline seawater

Yongqi Tian,[a] Yufang Yang,[a] Dongyan Zhong,[a] Shuangshuang Zhang,[a] Boyao Zhang,[a] Xin Li,[a] Huiya Zhou,[a] Rong-Da Zhao *[a] and Lihua Miao *[b]

Developing efficient and stable bifunctional electrocatalysts for overall water splitting, especially in practical electrolytes such as seawater, remains a significant challenge in the field of energy conversion. Herein, we report the successful synthesis of a three-dimensional, flower-like polymetallic phosphide electrocatalyst (Ru-CoVO-P), constructed from self-assembled ultrathin nanosheets, *via* a facile hydrothermal method combined with a low-temperature phosphidation strategy. The catalyst exhibits excellent bifunctional activity in 1 M KOH, requiring overpotentials of only 88.7 mV (HER) and 248.3 mV (OER) to achieve 10 mA cm^{-2}. After 240 hours of cycling in a two-electrode system, a cell voltage of only 1.753 V is required to achieve a current density of 50 mA cm^{-2}. More importantly, the catalyst maintains excellent performance in 1 M KOH containing seawater, demonstrating outstanding stability and great application potential. The superior performance stems from the electronic structure modulation among the polymetallic components, as well as the abundant active sites and efficient mass transport capabilities provided by the hierarchical structure. This work provides a facile and effective synthesis strategy for developing advanced polymetallic phosphide catalysts suitable for practical seawater electrolysis.

Received 11th July 2025
Accepted 4th September 2025

DOI: 10.1039/d5ra04957a

rsc.li/rsc-advances

1 Introduction

Economic development has significantly increased the demand for clean energy production and storage. As a clean energy source, hydrogen emits zero carbon dioxide during its utilization process, which has garnered substantial public attention.[1] In recent years, the water electrolysis method has emerged as a highly promising approach for hydrogen production. Electrochemical water splitting, which involves the hydrogen evolution reaction (HER) and the oxygen evolution reaction (OER), is one of the most promising and cost-effective pathways for producing green hydrogen fuel through overall electrochemical water decomposition.[2] However, the sluggish reaction kinetics and high reaction barriers in the electrolysis process necessitate highly active catalysts to reduce overpotential and enhance reaction rates. To date, Pt- and Ir-based compounds have demonstrated promising catalytic activity for HER and/or OER. However, their limited resource availability and cost inefficiency pose significant barriers to large-scale commercial deployment.[3–5]

Recently, numerous bifunctional catalysts based on Fe, Co, and Ni compounds have attracted significant research interest and have been extensively explored in energy-related fields.[6–9] Among these, Co-based compounds are recognized as a class of promising electrocatalytic materials for highly efficient water splitting.[10] Cobalt possesses half-filled and fully filled d-orbitals with moderate effective nuclear charge towards d-electrons. Its d-electron configuration can be tailored through the formation of oxides, hydroxides, phosphides, sulfides, and other derivatives, leading to continuous performance breakthroughs.[11–15] Among various cobalt-based materials, Co–P-based catalysts exhibit unique structural and compositional characteristics that are particularly favorable for water splitting.[16] For example, Zhu *et al.* reported a cobalt metal/cobalt phosphide/nitrogen-doped carbon composite catalyst with a hierarchical hollow structure, denoted as Co-Co_xP/NC, which exhibits excellent OER performance requiring an overpotential of only 287 mV to achieve a current density of 10 mA cm^{-2} in 1 M KOH.[17] Nevertheless, such catalytic performance remains unsatisfactory, particularly under high electrolysis current densities. Metal doping represents a favorable strategy to modify the electronic configuration of catalysts, thereby optimizing the binding strength with reaction intermediates.[18–21] Furthermore, the introduction of metal heteroatoms has been demonstrated to significantly enhance electrical conductivity, thereby facilitating charge

[a]*School of Materials Science and Engineering, Liaoning University of Technology, Jinzhou, 121001, P. R. China. E-mail: Rongdazhaoln@126.com*
[b]*School of Medical Information Engineering, Shenyang Medical College, Shenyang, Liaoning, 110043, P. R. China. E-mail: miaolihua@163.com*

transfer during the water electrolysis process.[22,23] These synergistic multimetallic strategies have led to significant performance improvements. For example, a CoFeP heterostructure fabricated by one-step phosphidation exhibits a porous structure and abundant active sites, delivering overpotentials of 127 mV (HER) and 266 mV (OER) at 10 mA cm^{-2} in alkaline media.[24]

Vanadium(v), an abundant transition metal belonging to the VB group, has attracted considerable attention for its applications in electrocatalysis.[25] VN and VC have been demonstrated to be effective for HER, while VOOH shows activity for OER.[26,27] The excellent electrical conductivity and stability of VN also favor its application as a catalyst or support material. Studies indicate that combining oxides with V and Co can produce efficient OER-active catalysts.[28,29] V–Co-based catalysts, such as α-$CoVO_x$ and V-doped Co_3O_4, have been developed as promising candidates for OER electrocatalysis. The α-$CoVO_x$ catalyst exhibits excellent OER performance with a low overpotential of 254 mV required to achieve a current density of 10 mA cm^{-2}.[30,31] On the other hand, ruthenium (Ru) is an inexpensive noble metal, costing less than 5% of platinum per unit mass, and has demonstrated remarkable adsorption capabilities toward reaction intermediates, showing great potential for electrochemical HER.[32–35] Therefore, incorporating a small amount of Ru into cobalt-based catalyst systems could serve as an effective strategy to significantly enhance catalytic activity without substantially increasing the overall cost, thereby facilitating large-scale industrial applications.[36,37] The effectiveness of this strategy has been confirmed in recent studies. For example, by doping Ru into cobalt selenide with a special hollow microarray structure (Ru-c-$CoSe_2$), a remarkably low overpotential of only 97 mV is required to achieve a hydrogen evolution current density of 10 mA cm^{-2} in alkaline medium (1 M KOH), demonstrating the significant potential of Ru doping in promoting hydrogen evolution reaction kinetics.[38] Despite these advances, the mechanistic understanding of multimetallic phosphides remains limited. It is still unclear how doping with noble metals like Ru alters the electronic structure of Co–V phosphide precursors or promotes dynamic surface reconstruction during the oxygen evolution reaction. Moreover, the origins of their high activity and stability in harsh environments such as seawater are not fully understood, hindering practical application.

We report a three-dimensional flower-like multimetallic phosphide electrocatalyst (Ru-CoVO-P) constructed from ultrathin nanosheets *via* self-assembly. This study aims to develop a bifunctional catalyst for overall water splitting by rationally integrating the properties of Ru, Co, V, and P, balancing high activity with cost-effectiveness. The primary objectives include: (1) presenting a facile, low-temperature strategy for synthesizing complex multimetallic phosphides; (2) achieving excellent performance in overall water splitting under high current densities in alkaline media; and (3) evaluating the long-term stability and practical application potential in simulated seawater, a more challenging environment. The resulting Ru-CoVO-P catalyst exhibits not only outstanding catalytic activity but also remarkable stability in both alkaline and seawater electrolytes.

2 Experimental section

2.1 Preparation of the precursor

The nickel foam was cut into 4 × 4 cm squares and pretreated by immersion in 3 M HCl for 30 minutes, followed by ultrasonic cleaning in deionized water for 10 minutes. Subsequently, 1.5 mmol of NH_4VO_3 and 2 mmol of $CoCl_2 \cdot 6H_2O$ were dissolved in 60 mL of deionized water, and the mixture was magnetically stirred until a transparent pink solution was formed. This solution, along with a piece of the pretreated nickel foam, was transferred into a 100 mL Teflon-lined autoclave. The autoclave was sealed and heated at 160 °C for 13 hours. After naturally cooling to room temperature, the nickel foam was retrieved, washed thoroughly with ethanol and deionized water, and finally dried at 60 °C for 6 hours to obtain the Co–V bimetallic catalyst precursor.

2.2 Preparation of Ru-CoVO-P catalyst

0.3 mmol of $RuCl_3 \cdot 3H_2O$ was dispersed in a water–ethanol mixed solvent (1 : 1, v/v). Under vigorous stirring, a 0.05 mmol $NaBH_4$ solution was rapidly added. A Ni foam loaded with the precursor was immersed in the mixture and reacted for 4 hours. The resulting sample was then thoroughly washed with ethanol and deionized water.[39] Subsequently, it was annealed at 350 °C for 120 minutes in a tube furnace under argon flow, with $NaH_2PO_2 \cdot H_2O$ (500 mg) placed upstream as a phosphorization source, and was designated as Ru-CoVO-P.

For comparison, the sample obtained without the annealing step was labeled Ru-CoVO-1; the sample obtained by immersing the precursor only in the $RuCl_3 \cdot 3H_2O$ solution was named Ru-CoVO-2; and the sample obtained by immersing the precursor solely in the $NaBH_4$ solution was marked as CoVO.

2.3 Preparation of the electrocatalyst

The phase composition and crystal structure of the obtained products were analyzed by X-ray diffraction (XRD, Shimadzu-7000, Cu Kα). The elemental composition of the samples was investigated using X-ray photoelectron spectroscopy (XPS, ESCALAB 250, Al-Kα). Scanning electron microscopy (SEM, Gemini 300-71-31) was employed to observe the surface morphology of the synthesized samples. Transmission electron microscopy (TEM, JEM-2100 PLUS) was further employed to analyze the internal microstructure and lattice fringes of the product.

2.4 Electrocatalytic performance testing

The electrocatalytic performance of the synthesized product was evaluated using a standard three-electrode system on a CHI760E electrochemical workstation (Shanghai Chenhua). The fabricated product (0.5 × 0.5 cm) was utilized as the working electrode, with Hg/HgO as the reference electrode, a carbon rod as the counter electrode for the HER, and a platinum sheet electrode as the counter electrode for the OER. The

electrolyte solutions used were 1 M KOH (pH = 13.7) and a mixture of 1 M KOH and seawater (pH = 13.51). The electrocatalytic measurements included linear sweep voltammetry (LSV), cyclic voltammetry (CV), Electrochemical Impedance Spectroscopy, (EIS), and cyclic stability tests. The LSV curves were corrected with 90% IR compensation, and the potential was converted to the reversible hydrogen electrode (RHE) using the Nernst equation: $E_{RHE} = E_{Hg/HgO} + 0.059 \times pH + 0.098$. The OER overpotential was calculated using $\eta = E_{RHE} - 1.23$ V.

3 Results and discussion

3.1 Structural and morphological characterization

First, the phase composition of the prepared samples was characterized by XRD. The XRD pattern of the precursor sample, CoVO, exhibits a series of sharp diffraction peaks, all of which match the standard pattern for cobalt vanadate (PDF#97-042-0769). In the XRD patterns of Ru-CoVO-1 and Ru-CoVO-2, characteristic diffraction peaks belonging to RuO_2 (PDF#97-023-6963) appeared at 27.68°, 34.69°, and 53.6°, indicating the successful incorporation of RuO_2. Following a phosphidation treatment, the XRD pattern of the sample Ru-CoVO-P changed significantly. The diffraction peaks corresponding to CoVO disappeared and were replaced by several broad, diffuse peaks, indicating a significant structural reconstruction during the phosphidation process. In the XRD pattern of Ru-CoVO-P, the main diffraction peaks located at 13.17°, 20.03°, 28.47°, 31.49° and 33.46° can be indexed to the (002), (110), (200), (202) and (114) crystal planes of $Co(VO)_2(PO_4)_2(H_2O)_4$ (PDF#97-006-7659), respectively, indicating the formation of a new phase after phosphidation. Furthermore, weaker diffraction peaks attributable to RuO_2 (PDF#97-002-3961) could still be observed at 28.07°, 35.09°, and 54.37°, suggesting that the RuO_2 species was preserved during the phosphidation process.

To gain deeper insights into the surface chemical composition and oxidation states of the prepared electrocatalyst, XPS was performed. The Co 2p spectrum of Ru-CoVO-P can be deconvoluted into seven peaks (Fig. 1b). Two main peaks corresponding to Co $2p_{3/2}$ and Co $2p_{1/2}$ exhibit a spin–orbit splitting of 15.8 eV, accompanied by two shake-up satellite peaks.[40–42] The peak at 774.7 eV can be attributed to Co^0, indicating that some Co ions on the material's surface were reduced to metallic Co under argon atmosphere, which is beneficial for enhancing the material's electrical conductivity and improving electron transfer during electrochemical processes. Peaks at 781.4/797.2 eV and 784.9/800.9 eV correspond to Co^{3+} and Co^{2+}, respectively, while peaks at 787.8 eV and 803.8 eV represent the satellite peaks of Co. The V 2p core-level spectrum (Fig. 1c) is fitted with two peaks at 516.7 eV for V $2p_{3/2}$ and 523.9 eV for V $2p_{1/2}$.[43] Peaks located at 515.9 eV and 522.9 eV belong to V^{4+}, whereas those at 516.7 eV and 524.3 eV correspond to V^{5+}. Fig. 1d shows three characteristic peaks in the O 1s spectrum. Specifically, the peak at a binding energy of 533.3 eV is typically associated with low-coordination oxygen ions on the surface.[44] The peak at 531.6 eV corresponds to chemisorbed and physisorbed water molecules on and within the surface, while the peak at 530.2 eV is attributed to defective oxygen.[45,46] Fig. 1e shows the high-resolution Ru 3p spectrum, where two distinct peaks appear at 461.4 eV and 485.7 eV, corresponding to Ru $3p_{3/}$

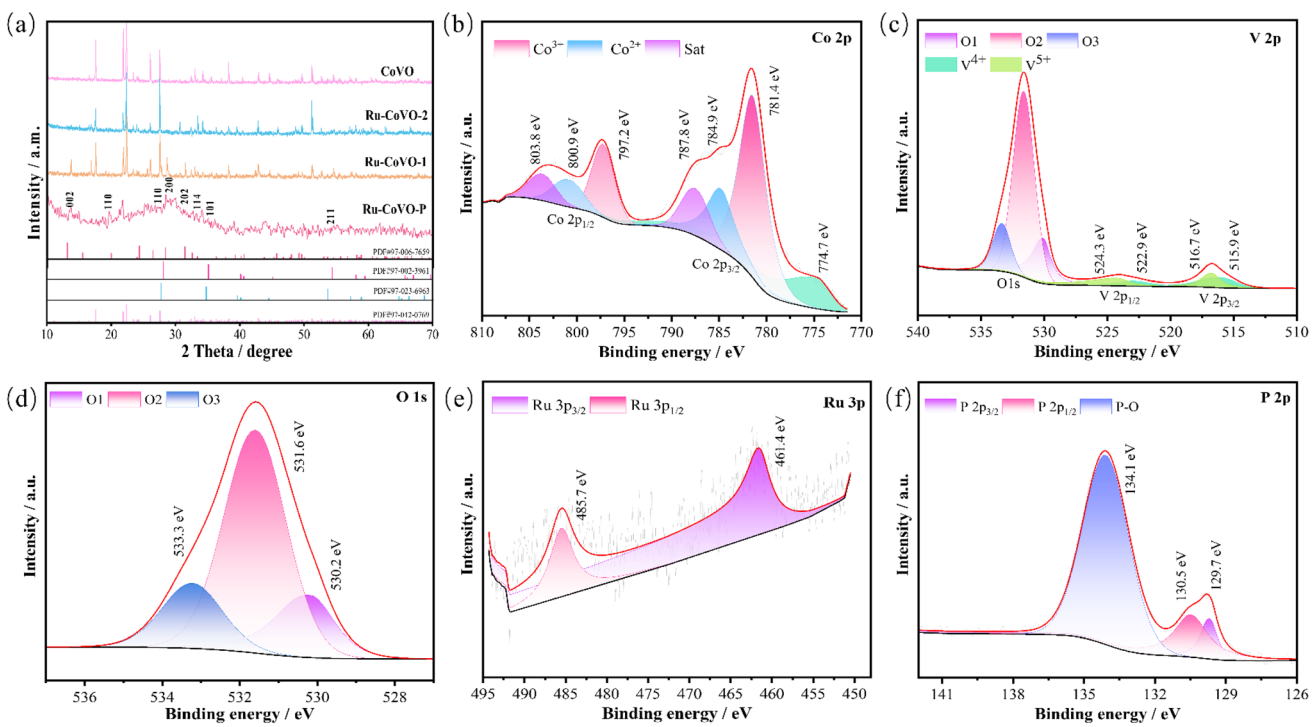

Fig. 1 Structure characterization of as-fabricated samples. (a) XRD patterns of the as prepared samples (b) XPS of Co 2p (c) V 2p (d) O 1s (e) Ru 3p (f) P 2p.

$_2$ and Ru $3p_{1/2}$, respectively. This confirms that the Ru dopant has been successfully incorporated into the Ru-CoVO-P catalyst.[47] The introduction of Ru significantly modulates the electronic structure of Co and V atoms, which may optimize the adsorption behavior of oxygen-containing intermediates, thereby enhancing the electrocatalytic activity. The P–O peak is observed at 134.1 eV, while the P $2p_{1/2}$ and P $2p_{3/2}$ peaks are located at 130.5 eV and 129.7 eV, respectively (Fig. 1f). The presence of the P–O peak indicates partial surface oxidation of the sample, which is consistent with previous reports.[48]

To investigate the micro-morphology and elemental composition of the prepared Ru-CoVO-P catalyst, we performed SEM and EDS characterizations. The SEM image (Fig. 2a) clearly reveals that the catalyst forms a uniform and dense film on the substrate, composed of a large number of uniformly sized, three-dimensional flower-like microspheres. Further magnification (Fig. 2b) shows that these unique flower-like microspheres are self-assembled from countless ultrathin nanosheets as basic units, which are interconnected and oriented almost perpendicularly to the core. This open and porous hierarchical nanostructure not only greatly increases the specific surface area of the material, providing abundant contact interfaces and active sites for catalytic reactions, but also features interconnected pore channels that facilitate rapid electrolyte penetration and efficient detachment of generated gas bubbles (*e.g.*, O_2 and H_2), thereby significantly reducing mass transport limitations and ensuring sustained, high-performance operation of the catalyst. The morphologies of the other samples are shown in Fig. S1a–c. The low-magnification TEM image (Fig. S1d) clearly reveals that the catalyst is composed of ultrathin nanosheets as fundamental units. These intertwined nanosheets create a large surface area, providing abundant interfaces for the electrocatalytic reaction. To further probe the crystal structure, high-resolution TEM (HRTEM) was performed (Fig. S1e). The image shows well-defined, ordered lattice fringes, and upon measurement and indexing, the interplanar spacings of $d = 0.2676$ nm and $d = 0.2551$ nm are found to correspond to the (114) plane of $Co(VO)_2(PO_4)_2(H_2O)_4$ and the (101) plane of RuO_2, respectively. The regular arrangement and spacing of these lattice fringes are further confirmed by the line profile analysis (Fig. S1f). To confirm the uniformity of its chemical composition, EDS elemental mapping analysis was conducted on the Ru-CoVO-P sample (Fig. 2c). The results show that the main elements constituting the framework Co, V, O, P and Ru are all highly uniformly distributed, with no obvious elemental aggregation or segregation. In summary, this three-dimensional hierarchical network structure with a high specific surface area, combined with the uniform dispersion of multiple elements, constitutes the unique advantages of this catalyst.

3.2 Electrocatalytic performance of the catalyst in 1 M KOH

The OER performance of the catalyst was systematically evaluated in 1 M KOH electrolyte. After 30 CV activation cycles, LSV measurements were conducted at a scan rate of 2 mV s^{-1} (Fig. 3a). The results showed that commercial IrO_2 exhibits the best performance at a current density of 10 mA cm^{-2}. Notably, the performance advantage of Ru-CoVO-P becomes more pronounced at higher current densities. Under higher current density conditions, its overpotential gradually approaches and ultimately surpasses that of IrO_2. Specifically, Ru-CoVO-P achieves remarkably low overpotentials of 248.3 mV, 306.3 mV, and 338.3 mV to deliver current densities of 10, 50, and 100 mA cm^{-2}, respectively (Fig. 3b), outperforming other catalysts.

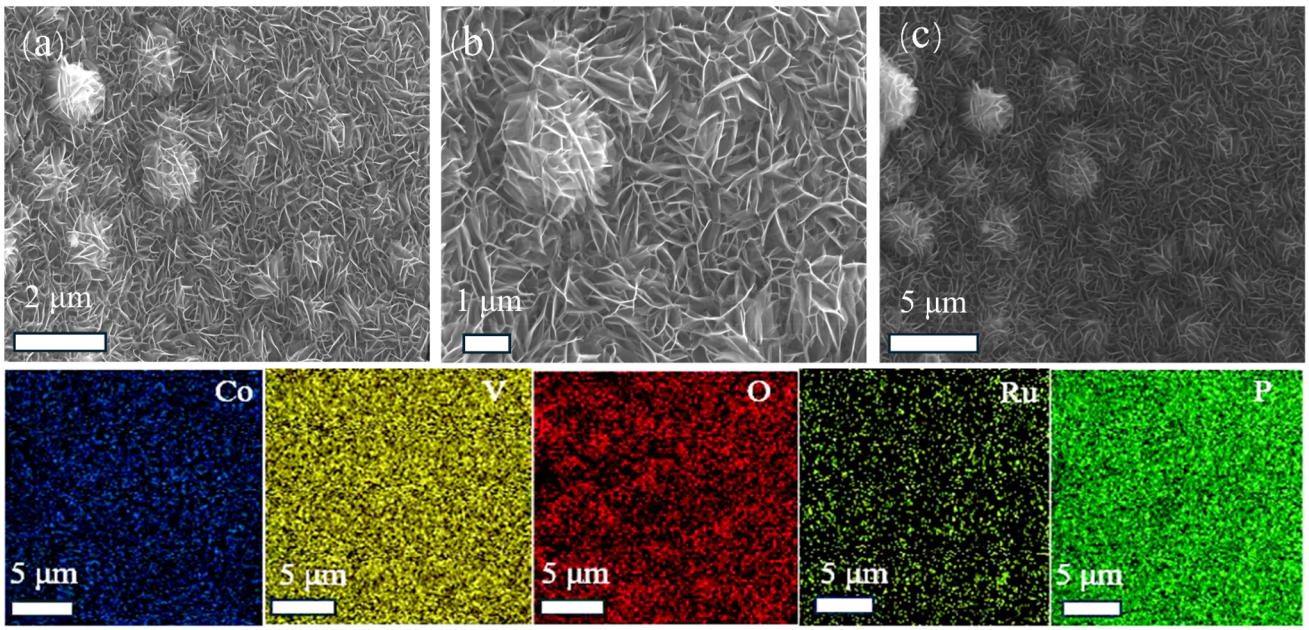

Fig. 2 Morphology and structure characterization of the as-prepared products (a and b) SEM images of Ru-CoVO-P (c) EDS elemental mapping of Co, V, O, Ru and P for Ru-CoVO-P.

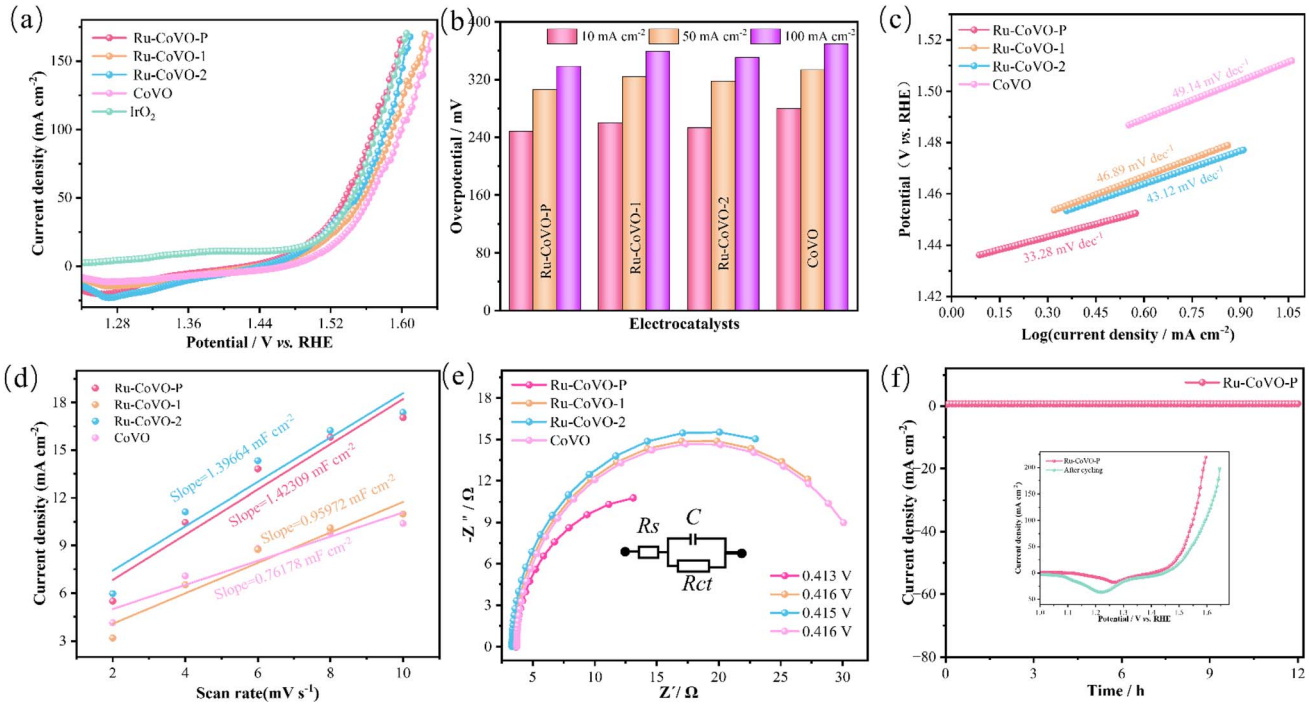

Fig. 3 OER performances in 1.0 KOH solutions (a) polarization curves at scan rate of 2 mV s^{-1} (b) overpotential of electrode materials (c) Tafel plots (d) double-layer capacitance (C_{dl}) (e) Nyquist plots (f) cycling stability.

Fig. 3c shows the Tafel plots derived from the LSV curves, which provide deeper insight into the reaction mechanism. Ru-CoVO-P exhibited the smallest Tafel slope of only 33.28 mV dec^{-1}, indicating the fastest OER reaction kinetics among the studied catalysts.[49] The linear fitting plot for the C_{dl}, derived from the CV curves (Fig. S2), is shown in Fig. 3d. The results indicated that Ru-CoVO-P possessed the largest C_{dl} value (1.42309 mF cm^{-2}), which corresponds to the highest ECSA. The ECSA ranking for the samples is as follows: Ru-CoVO-P > Ru-CoVO-2 > Ru-CoVO-1 >CoVO. In addition, EIS analysis (Fig. 3e) further reveals the charge transfer kinetics of the catalysts. The results show that Ru-CoVO-P has the smallest diameter of the Nyquist semicircle, and its fitted charge transfer resistance (R_{ct}) is only 21.72 Ω (Table S1), significantly lower than that of all the control samples. This indicates that Ru-CoVO-P possesses the fastest interfacial charge transfer rate, a conclusion consistent with its excellent electrochemical performance, including low overpotential and the smallest Tafel slope. As shown in Fig. 3f, the Ru-CoVO-P catalyst maintains stable catalytic performance over a 12 hours durability evaluation. The inset presents a comparison of the LSV curves before and after the constant-potential cycling test. The results reveal only minor degradation in OER activity after prolonged operation, suggesting that the surface active site structure and electron transport pathways of the catalyst remain highly stable throughout the electrochemical process. This further confirms the excellent long-term electrochemical stability of Ru-CoVO-P.

In a three-electrode system comprising a carbon rod as the counter electrode, Hg/HgO as the reference electrode, and the catalyst as the working electrode, the HER performance of the catalysts was evaluated. LSV measurements were recorded at a scan rate of 5 mV s^{-1} in 1.0 M KOH electrolyte. As shown in Fig. 4a, Ru-CoVO-P exhibits the closest performance to Pt/C among all samples. At a current density of −10 mA cm^{-2}, Ru-CoVO-P requires an overpotential of only 88.7 mV, significantly lower than those of Ru-CoVO-1 (126.7 mV), Ru-CoVO-2 (127.7 mV), and CoVO (149.7 mV). Notably, Ru-CoVO-P achieves a high current density of 50 mA cm^{-2} with a low overpotential of just 180.7 mV, highlighting the beneficial effect of Ru doping on HER activity. The electrochemical reaction kinetics can be further studied through Tafel slopes (Fig. 4b). The Tafel slopes for Ru-CoVO-P, Ru-CoVO-1, Ru-CoVO-2, and CoVO are 63.46 mV dec^{-1}, 66.02 mV dec^{-1}, 66.89 mV dec^{-1}, and 71.41 mV dec^{-1}, respectively. The lower Tafel slope of Ru-CoVO-P indicates favorable reaction kinetics. ECSA is a critical parameter for assessing the performance of electrocatalysts, representing the effective surface area involved in electrochemical reactions. Since ECSA is proportional to the C_{dl}, it can be determined by calculating C_{dl}. CV curves are provided in Fig. S3. As illustrated in Fig. 4c, Ru-CoVO-P has a double-layer capacitance value of 0.08821 mF cm^{-2}, significantly higher than that of other prepared catalysts. Fig. 4d clearly shows the differences among the four catalysts in terms of overpotential (for OER/HER), ECSA, and Tafel slope, visually demonstrating the superior performance of Ru-CoVO-P. To further understand the kinetic characteristics and reaction mechanisms at the catalyst interface, based on the above results, a comprehensive radar chart is plotted in Fig. 4d. This chart vividly illustrates the remarkable performance of Ru-CoVO-P as a candidate material, consistent with our predictions.

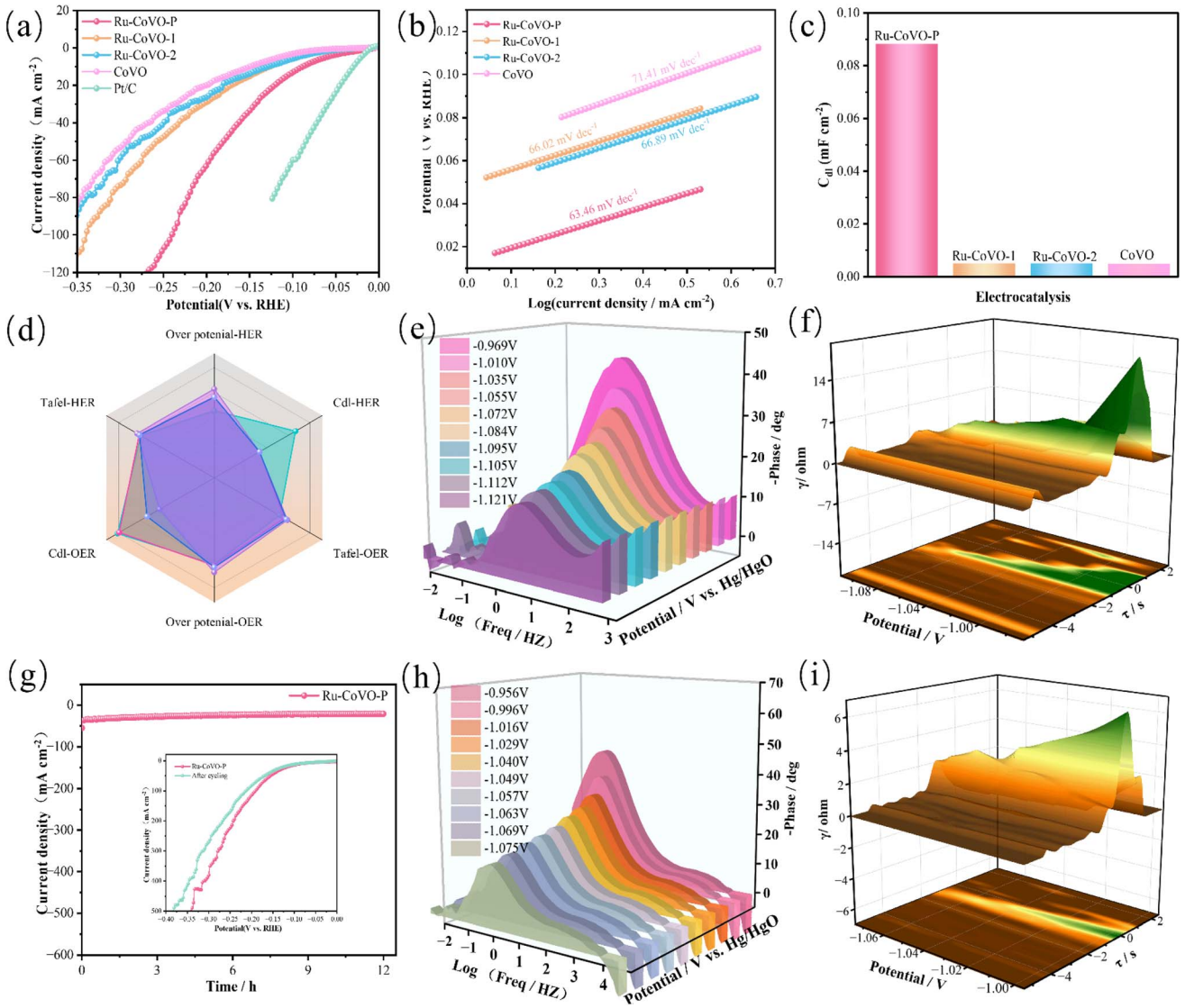

Fig. 4 HER performances in 1.0 KOH solutions (a) polarization curves at scan rate of 5 mV s^{-1} (b) Tafel plots (c) a bar chart of the double-layer capacitance (C_{dl}) values (d) radar chart (e) 3D Bode plot (f) DRT spectrum of Ru-CoVO-P sample (g) cycling stability (h) 3D Bode plot after cycling (i) DRT spectrum of Ru-CoVO-P sample after cycling.

In addition to catalytic activity, the dynamic response of the catalyst was investigated through three-dimensional Bode plots measured at varying potentials (from −5 mA cm^{-2} to −60 mA cm^{-2}) (Fig. 4e). The phase angle *versus* frequency curves reflect the dynamic response characteristics of the catalyst samples.[50] Fig. S6a presents the EIS fitting results at different overpotentials. As the cathodic overpotential increases (from −0.969 V to −1.121 V), the charge transfer resistance (R_{ct}) significantly decreases from 31.09 Ω to 3.271 Ω. The detailed fitting parameters are listed in Table S3. The reduction in R_{ct} demonstrates that higher overpotentials effectively accelerate charge transfer and HER kinetics, a trend consistent with the LSV results.[51,52] Together, these findings confirm the catalyst's excellent intrinsic electrocatalytic activity. Fig. 4f shows the Distribution of Relaxation Times (DRT) analysis of Ru-CoVO-P under HER conditions, revealing a distinct peak in the low-frequency region. As the applied potential becomes more negative, the intensity (γ/Ω) of this peak increases significantly. This low-frequency feature is attributed to mass transport processes. In high-rate hydrogen evolution, such processes are primarily governed by H_2 bubble dynamics, including nucleation, growth, and detachment from the electrode surface. Therefore, the pronounced rise in peak intensity with increasing overpotential indicates that bubble-induced mass transport resistance becomes the dominant contributor to overall electrode polarization at high current densities.

As the potential shifts negatively from −0.96 V to −1.08 V, the γ value of the mid-frequency peak decreases significantly. This suggests that the increased overpotential provides a stronger driving force for HER, accelerating the reaction kinetics and reducing charge transfer resistance. In the high-frequency region, the polarization resistance (γ value) remains

relatively small with minimal variation across potentials, likely associated with the intrinsic charge transport properties of the electrode material itself.[53,54] Durability is another critical parameter for assessing catalyst performance. The Ru-CoVO-P catalyst retains high activity over a 12 hours continuous operation at a current density of 40 mA cm^{-2} in 1.0 M KOH electrolyte (Fig. 4g). The inset displays an overpotential comparison before and after the durability test, revealing no significant difference in overpotential values. This demonstrates that the catalyst exhibits excellent durability, sustaining stable current output during long-term continuous operation. The post-cycling Bode plot (Fig. 4h) reveals more ordered phase angle alignment after cycling, further highlighting the excellent charge transport efficiency of Ru-CoVO-P. Fig. 4i presents the DRT analysis after long-term cycling. Notably, a leftward shift toward higher frequencies and movement of characteristic peaks are observed, indicating that Ru-CoVO-P likely exhibits reduced impedance contribution and lower charge transfer resistance following extended stability testing. This undoubtedly benefits charge transport efficiency. Table 1 compares the electrocatalytic performance of the prepared samples with previously reported catalysts, showing that Ru-CoVO-P exhibits lower overpotentials than other currently reported catalysts.

XPS analysis was performed on the Ru-CoVO-P catalyst after cycling. The results (Fig. 5a) show that after long-term electrochemical testing, the characteristic peaks of all core elements (Co, V, Ru, P, O) on the catalyst surface remain clearly discernible. This indicates that the catalyst's fundamental framework and surface elemental composition remained largely intact, without significant dissolution or loss. The high-resolution XPS spectrum of Co 2p (Fig. 5b) reveals that the characteristic peaks shifted overall toward lower binding energies after cycling. This can be attributed to the partial reduction of high-valence active sites, such as Co^{3+}, to lower oxidation states like Co^{2+}.[55] Concurrently, the disappearance of the V^{5+} characteristic peak in the V 2p spectrum after cycling (Fig. 5c) suggests that V^{5+} was almost completely reduced to V^{4+}. This is related to the formation of oxygen vacancies.[56] These defective sites facilitate the adsorption and dissociation of water molecules, thereby accelerating the formation of the (oxy)hydroxide active layer. The resulting low-valent Co and V ions serve as ideal precursors for the *in situ* generation of highly active Co/V–OOH species under anodic potentials. The O 1s spectrum (Fig. 5d) shows that after cycling, the peak area corresponding to surface hydroxyl groups (–OH) at higher binding energies increases significantly and becomes the dominant peak, while the peak representing bulk lattice oxygen (M–O) at lower binding energies decreases markedly. This clearly indicates substantial hydroxylation on the catalyst surface, forming a surface layer rich in hydroxides. Correspondingly, in the Ru 3p spectrum (Fig. 5e), the characteristic peaks for Ru $3p_{3/2}$ and Ru $3p_{1/2}$ shift towards higher binding energies, reaching 463.9 eV and 486.4 eV, respectively. This positive shift suggests significant oxidation of ruthenium on the catalyst surface. Ru atoms are oxidized to form high-valent RuO_x species, which serve as highly active sites due to their favorable binding energy with oxygen-containing intermediates. Meanwhile, they modulate the electronic structure of neighboring Co and V atoms through an electron-withdrawing effect, accelerating the reaction kinetics. Furthermore, the incorporation of Ru enhances charge transfer efficiency and stabilizes the surface (oxy)hydroxide layer, thereby significantly boosting the catalytic activity and stability of the catalyst. In contrast, the P 2p spectrum (Fig. 5f) shows that the characteristic peak for P–O bonds remains dominant both before and after cycling. This strongly confirms the high chemical stability of phosphate groups during the process.

However, the finite and geographically disparate distribution of freshwater resources contrasts sharply with that of seawater. Constituting 96.5% of the Earth's water resources, seawater presents a sustainable alternative for electrolytic processes.[57–59] Therefore, in our subsequent work, we conducted electrochemical tests on the samples in an alkaline electrolyte environment using 1 M KOH + seawater.

3.3 Electrocatalytic performance of the catalyst in 1 M KOH + seawater

To evaluate the OER performance of the catalyst in seawater, a series of electrochemical tests were conducted. As shown in Fig. 6a and b, the Ru-CoVO-P catalyst exhibits excellent OER

Table 1 Comparison of electrochemical properties of Ru-CoVO-P electrode materials with previous literature

Electrode materials	Electrolyte	Overpotential (mV)	Tafel slope (mV dec^{-1})	Reference
Ru-CoVO-P	1 M KOH	OER-248.3 (10 mA cm^{-2})	33.28	This work
		HER-88.7 (−10 mA cm^{-2})	63.46	
$CoVO_x$	1 M KOH	OER-308 (10 mA cm^{-2})	62	64
Ru@NiCo-MOF	1 M KOH	OER-284 (10 mA cm^{-2})	78.82	65
Ru-Co_3O_4/CoP/TM	1 M KOH	OER-293 (10 mA cm^{-2})	74.8	66
		HER-47 (−10 mA cm^{-2})	93	
RuCoP/NF	1 M KOH	OER-385 (50 mA cm^{-2})	89.7	67
		HER-49 (−10 mA cm^{-2})	159.1	
NiFe LDH/NiS_2/VS_2	1 M KOH	OER-286 (10 mA cm^{-2})	99	68
		HER-76 (−10 mA cm^{-2})	79	
Ru-CoV-LDH/NF	1 M KOH	OER-230 (10 mA cm^{-2})	81.2	69
		HER-32 (−10 mA cm^{-2})	36.4	

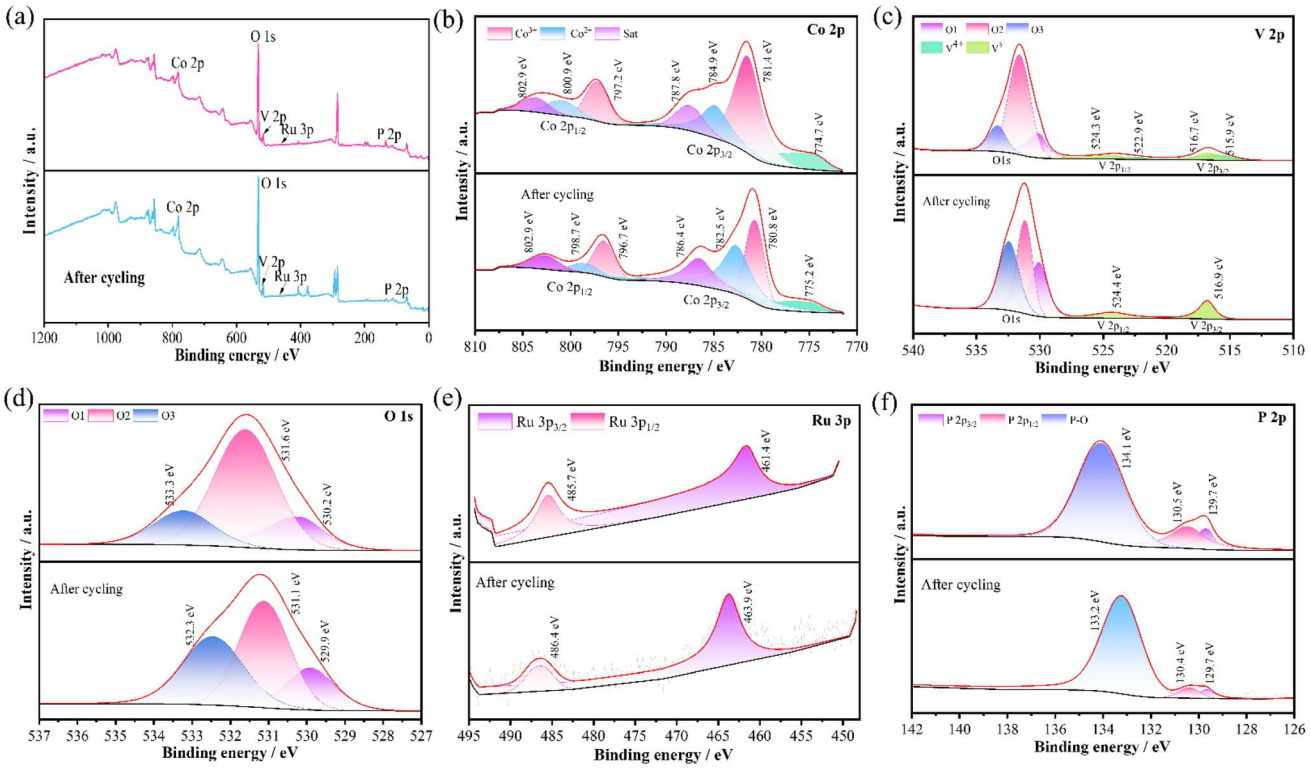

Fig. 5 (a) The high resolution XPS Survey spectra before and after cycling. (b)XPS of Co 2p (c) V 2p (d) O 1s (e) Ru 3p (f) P 2p.

activity. At a benchmark current density of 10 mA cm^{-2}, it requires an overpotential as low as 199.5 mV, significantly outperforming Ru-CoVO-1 (241.5 mV), Ru-CoVO-2 (244.5 mV), and CoVO (268.5 mV). Moreover, even at high current densities of 50 and 100 mA cm^{-2}, Ru-CoVO-P achieves low overpotentials of only 274.5 mV and 307.5 mV, respectively, demonstrating its

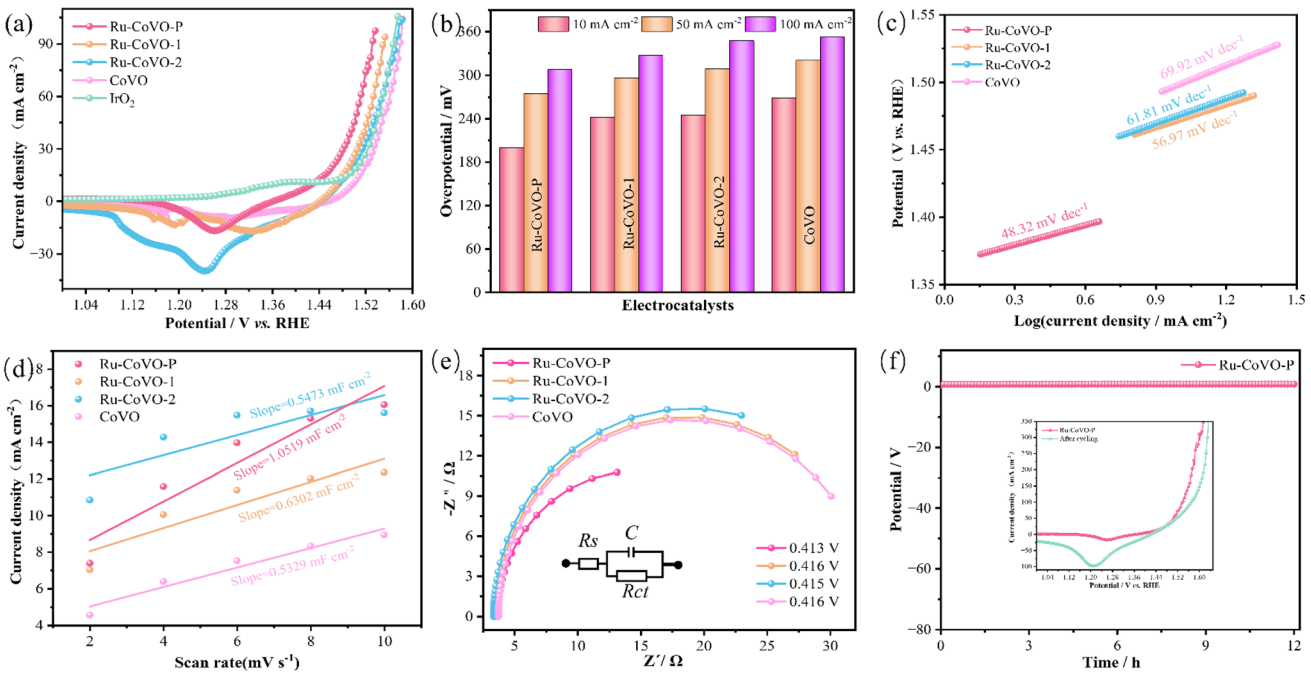

Fig. 6 OER performances in 1.0 KOH + seawater solutions (a) polarization curves at scan rate of 2 mV s^{-1} (b) overpotential of electrode materials (c) Tafel plots (d) double-layer capacitance (C_{dl}) (e) Nyquist plots (f) cycling stability.

great potential for operation under high-current conditions. Through Tafel slope analysis (Fig. 6c), we investigated the reaction kinetics. The Tafel slope for Ru-CoVO-P is only 48.32 mV dec^{-1}, significantly lower than those of the other comparative materials. This indicates that the introduction of Ru and P greatly enhances its intrinsic catalytic activity. To quantify the number of active sites, we calculated the C_{dl} and ECSA using cyclic voltammetry (Fig. 6d). According to the formula ECSA = (C_{dl}/0.04 mF cm^{-2}), the ECSA of Ru-CoVO-P is calculated to be 26.297 cm^2, which is significantly higher than that of Ru-CoVO-1 (15.755 cm^2), Ru-CoVO-2 (13.682 cm^2), and CoVO (13.322 cm^2). This indicates that Ru-CoVO-P possesses a larger electrochemically active surface area and exposes more active sites. EIS further reveals kinetic information at the electrode/electrolyte interface. The OER kinetics of the Ru-CoVO-P catalyst in simulated seawater were further validated by EIS measurements (Fig. 6e). As shown in the fitted data (Table S2), it exhibits the lowest charge transfer resistance (R_{ct}) among all samples, with a value of only 11.66 Ω. This indicates that the excellent charge transfer capability of Ru-CoVO-P remains intact even in the complex ionic environment, maintaining highly efficient reaction kinetics. Finally, a 12 hours continuous chronoamperometric (i–t) test (Fig. 6f) demonstrates that the current density of Ru-CoVO-P remains stable with no significant decay. The comparison of polarization curves before and after the test, as shown in the inset of Fig. 6f, also reveals almost no increase in overpotential, strongly confirming the exceptional long-term operational stability of the catalyst.

We conducted an in-depth study on its HER performance in seawater following the evaluation of its excellent OER performance. As shown in Fig. 7a, Ru-CoVO-P exhibits remarkable activity and a low onset potential, delivering low overpotentials of 134.5 mV and 250.5 mV to achieve current densities of 10 mA cm^{-2} and 50 mA cm^{-2}, respectively. This indicates that the introduction of Ru and P can further fine-tune the electronic

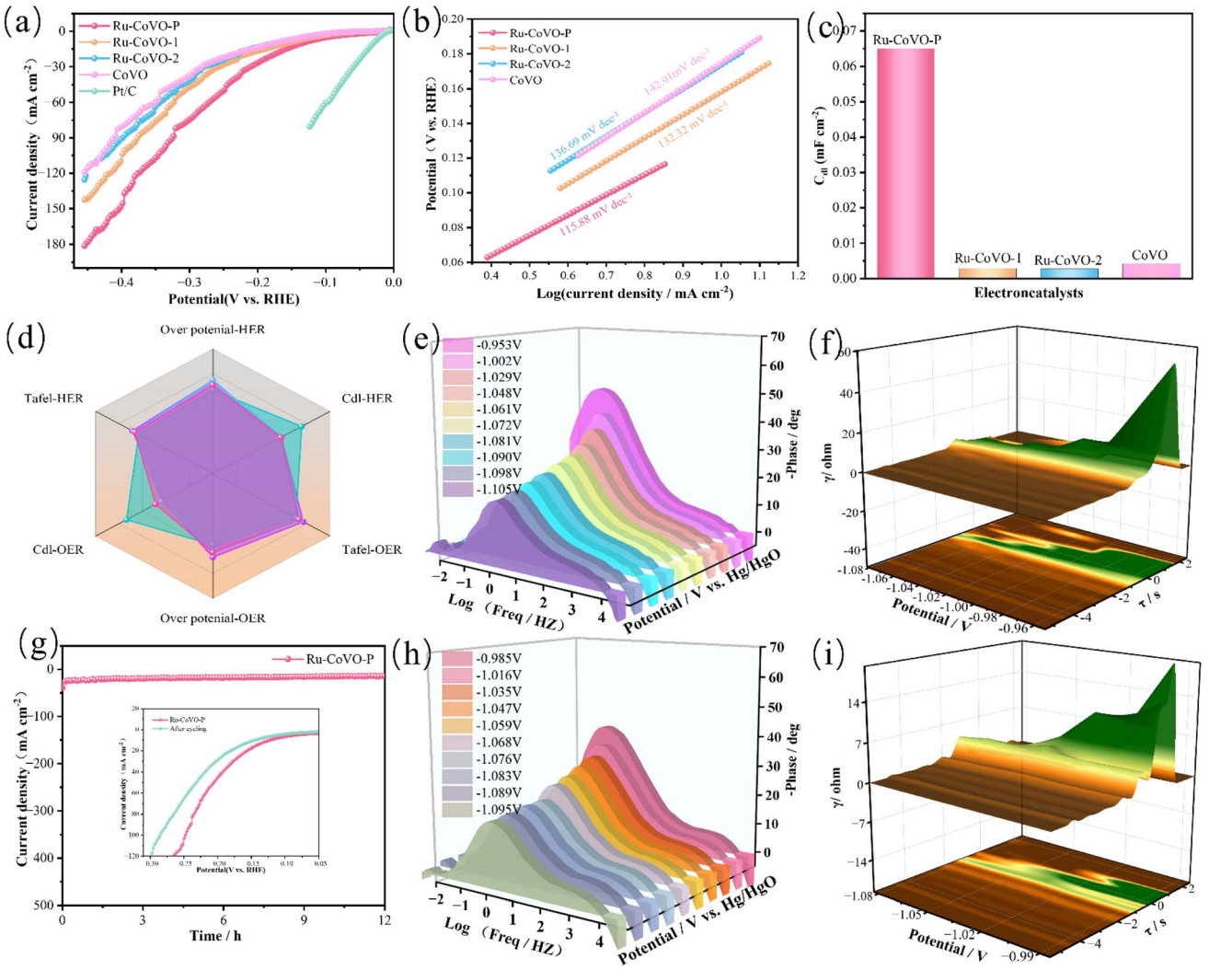

Fig. 7 HER performances in 1.0 KOH + seawater solutions (a) polarization curves at scan rate of 5 mV s^{-1} (b) Tafel plots (c) a bar chart of the double-layer capacitance (C_{dl}) values (d) radar chart (e) 3D Bode plot (f) DRT spectrum of Ru-CoVO-P sample (g) cycling stability (h) 3D Bode plot after cycling (i) DRT spectrum of Ru-CoVO-P sample after cycling.

structure of Co and V sites, effectively enhancing catalytic activity. The Tafel slope of Ru-CoVO-P is 115.88 mV dec^{-1}, which is lower than those of Ru-CoVO-1, Ru-CoVO-2, and CoVO at 132.32 mV dec^{-1}, 136.89 mV dec^{-1}, and 142.91 mV dec^{-1}, respectively (Fig. 7b). This demonstrates that Ru-CoVO-P possesses superior electrocatalytic kinetics and the highest catalytic activity. To further validate and explore the source of Ru-CoVO-P′s superior performance. As shown in Fig. 7c, the C_{dl} value of Ru-CoVO-P is approximately 0.065 mF cm^{-2}, while those of Ru-CoVO-1, Ru-CoVO-2, and CoVO are all below 0.005 mF cm^{-2}. This indicates that Ru-CoVO-P possesses abundant active sites. Fig. 7d presents a comprehensive performance radar chart of the catalysts in seawater. It clearly shows that Ru-CoVO-P exhibits the best overall performance for water splitting. Fig. 7e presents the three-dimensional Bode plots of Ru-CoVO-P at various potentials, aiming to elucidate the HER kinetic mechanism. With increasing overpotential, a notable shift of the phase angle peak toward higher frequencies is observed, directly confirming that the HER reaction rate accelerates due to a decrease in charge transfer resistance (R_{ct}). Moreover, the emergence of a second time constant feature in the low-frequency region indicates that HER proceeds through a multi-step process involving adsorbed hydrogen intermediates (H_{ads}), suggesting a possible reaction pathway following either the Volmer–Heyrovsky or Volmer–Tafel mechanism. As shown in Fig. S6b and Table S4, Ru-CoVO-P exhibits excellent charge transfer kinetics despite various coexisting ions. R_{ct} decreases significantly from 42.9 Ω to 5.305 Ω as the cathodic overpotential increases from −0.953 V to −1.105 V (*vs.* RHE), indicating enhanced HER kinetics at higher driving forces.[60] This robust performance in a complex ionic environment highlights the catalyst's practical potential. To further interpret the complex dynamic processes observed in the Bode plots, we introduced the DRT analysis (Fig. 7f). The DRT spectra intuitively reveal that as the applied potential becomes more negative, the high-frequency peak associated with charge transfer resistance (R_{ct}) decreases dramatically. This precisely explains why the main peak in the Bode plot shifts toward higher frequencies. Meanwhile, the resistance corresponding to hydrogen adsorption in the low-frequency region also

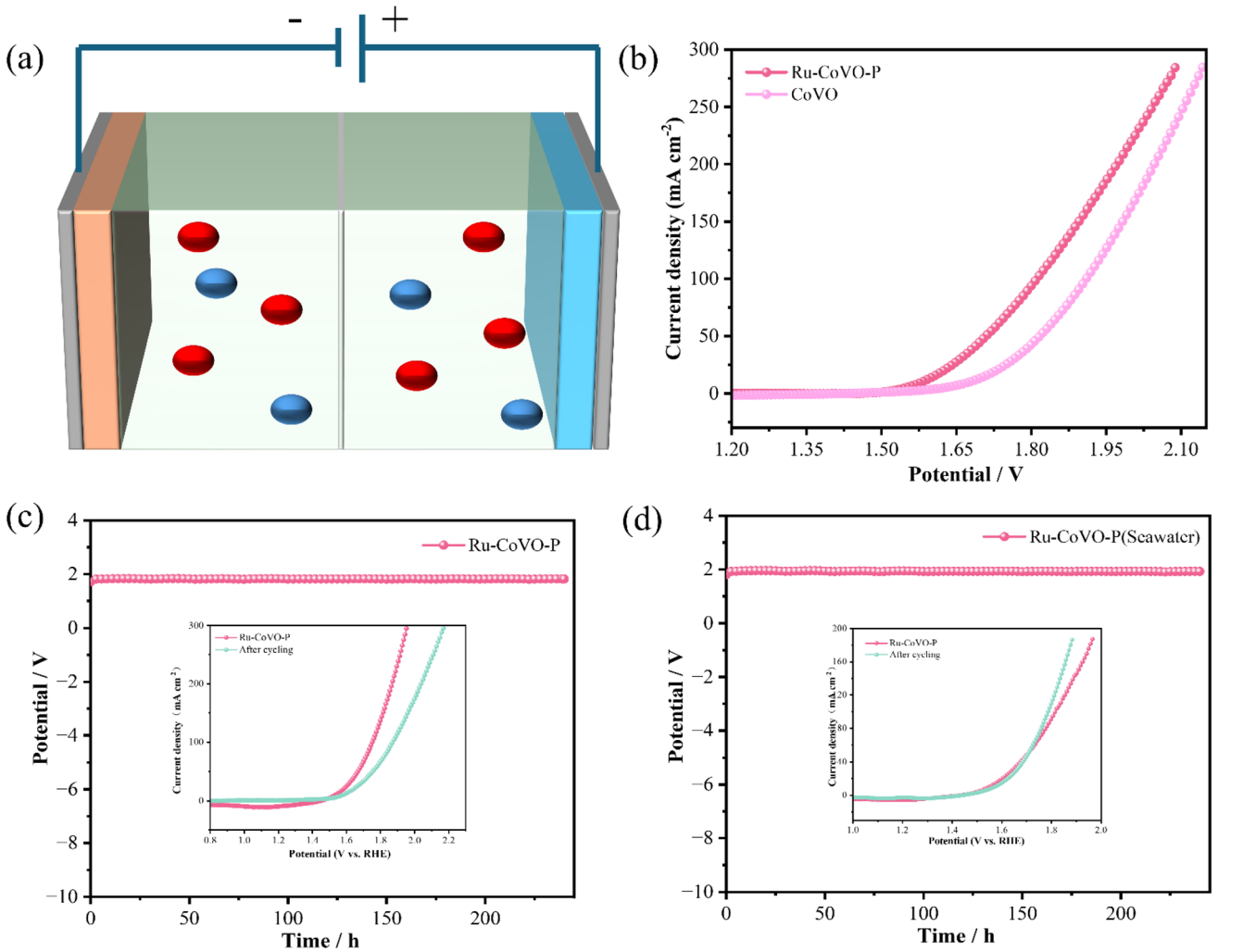

Fig. 8 Overall water splitting performance of the electrocatalysts (a) device schematic diagram (b) LSV curves in 1.0 M KOH solution (c) cycling stability in 1.0 M KOH (d) cycling stability in 1.0 M KOH + seawater.

diminishes, indicating that the entire reaction pathway is effectively facilitated. A long-term galvanostatic (Fig. 7g) operation further verifies the outstanding stability of the prepared sample. The inset shows the LSV curves of Ru-CoVO-P before and after cycling. After 12 hours of operation, no significant increase in overpotential is observed. Post-cycling Bode and DRT analyses (Fig. 7h and i) demonstrate that the enhanced catalytic activity originates from reduced resistances in both the charge transfer and hydrogen adsorption steps, thereby accelerating the overall electrocatalytic kinetics.

The enhanced OER performance in alkaline seawater can be attributed to the synergistic effects of the highly alkaline environment: the competing chlorine evolution reaction (ClER) is effectively suppressed, while the elevated OH^- concentration directly facilitates the OER process.[61] In contrast, the HER performance shows significant deterioration primarily due to the complex ionic environment of seawater. During HER operation, the localized pH increase near the cathode triggers the precipitation of cations (particularly Mg^{2+} and Ca^{2+}), forming insoluble blocking layers of $Mg(OH)_2$ and $CaCO_3$. These insulating deposits progressively cover and deactivate the catalytic sites, ultimately compromising both the efficiency and long-term stability of hydrogen generation.[62,63]

3.4 Overall water splitting performance of the catalyst

To explore the practical application potential of the electrocatalyst, overall water splitting tests were carried out in a two-electrode system. The corresponding schematic diagram is shown in Fig. 8a, where OER takes place at the anode with OH^- oxidized to O_2, and HER occurs at the cathode through the reduction of H^+ to H_2. Fig. 8b displays the LSV curves of the catalysts. It can be observed that the Ru-CoVO-P catalyst is capable of driving water splitting at a lower cell voltage and delivers a higher current density under the same applied potential, indicating enhanced catalytic activity and improved energy efficiency for hydrogen and oxygen production. To visually evaluate the gas management capability of the electrodes during the overall water splitting process, an *in situ* video was recorded for the two-electrode system using Ru-CoVO-P as both the cathode and anode (SI Movie S1). The video clearly shows the generation of a large number of dense and fine bubbles on the electrode surfaces. These microbubbles detach rapidly after their formation with almost no residence or coalescence on the surface, which is a typical characteristic of a superaerophobic surface. This efficient bubble detachment ensures that the catalyst's active sites are not covered or blocked by an insulating bubble layer, thus maintaining continuous and intimate contact between the electrolyte and the catalyst surface. This is crucial for sustaining stable catalytic activity at high current densities. The long-term stability of Ru-CoVO-P was evaluated through a 240 hours cycling test in 1 M KOH solution (Fig. 8c). The results show that the potential required to drive the reaction remained highly stable, exhibiting excellent durability. This result is further confirmed by the LSV curves before and after the test, and the potential increased only slightly to 1.753 V at a current density of 50 mA cm^{-2} after cycling. Notably, the catalyst still exhibited significant stability in the more challenging 1 M KOH + seawater, where the potential remained stable and the LSV curves were essentially unchanged (Fig. 8d). This indicates that the catalyst can maintain good structural integrity and high catalytic activity even in the presence of corrosive chloride ions, demonstrating its broad prospects for practical applications.

4 Conclusion

In summary, this work demonstrates the successful fabrication of Ru-CoVO-P polymetallic phosphide electrocatalysts supported on nickel foam (NF), featuring ultrathin nanosheet structures. This unique morphology affords a vast electrochemical active surface area and facilitates efficient charge and mass transport. Consequently, Ru-CoVO-P demonstrates exceptional bifunctional activity in 1 M KOH, requiring low overpotentials of just 248.3 mV for the OER and 88.7 mV for the HER to achieve a current density of 10 mA cm^{-2}. The catalyst maintains high efficiency and remarkable long-term stability in simulated seawater, underscoring its potential for application in corrosive environments. The outstanding performance is attributed to the synergistic electronic effects among its metallic components and the *in situ* formation of dynamic active species during electrolysis. This work provides a robust strategy for developing efficient, stable, and low-precious-metal bifunctional water-splitting catalysts.

Conflicts of interest

The authors declare no conflict of interest.

Data availability

The data that supports the findings of this study is available from the corresponding authors upon reasonable request.

Supplementary information is available. See DOI: **https://doi.org/10.1039/d5ra04957a**.

Acknowledgements

This work was supported by the Project of Education Department of Liaoning Province (No. LJKMZ20220959), the National Natural Science Foundation of China (No. 51971106). Science and Technology Innovation Talent Project of Liaoning Provincial Department of Education (LJ222411632049, LJ222411632081).

References

1 B. Mendoza-Sánchez and Y. Gogotsi, Synthesis of two-dimensional materials for capacitive energy storage, *Adv. Mater.*, 2016, **28**(29), 6104–6135.

2 S. Huang, Y. Meng, S. He, *et al.*, N^-, O^-, and S-tridoped carbon-encapsulated Co9S8 nanomaterials: efficient bifunctional electrocatalysts for overall water splitting, *Adv. Funct. Mater.*, 2017, **27**(17), 1606585.

3 B. X. Tao, X. L. Li, C. Ye, *et al.*, One-step hydrothermal synthesis of cobalt–vanadium based nanocomposites as bifunctional catalysts for overall water splitting, *Nanoscale*, 2019, **11**(39), 18238–18245.
4 K. Zeng, X. Zheng, C. Li, *et al.*, Recent advances in non-noble bifunctional oxygen electrocatalysts toward large-scale production, *Adv. Funct. Mater.*, 2020, **30**(27), 2000503.
5 J. Chen, J. Huang, R. Wang, *et al.*, Atomic ruthenium coordinated with chlorine and nitrogen as efficient and multifunctional electrocatalyst for overall water splitting and rechargeable zinc-air battery, *Chem. Eng. J.*, 2022, **441**, 136078.
6 H. Ren, Z. Zhang, S. Xu, *et al.*, Design and fabrication of high-performance $ZnCo_2O_4/ZnWS_4$ composite electrode materials for advanced asymmetric supercapacitors, *Ionics*, 2025, 1–14.
7 C. Ye, M. Q. Wang, G. Chen, *et al.*, One-step CVD synthesis of carbon framework wrapped Co2P as a flexible electrocatalyst for efficient hydrogen evolution, *J. Mater. Chem. A*, 2017, **5**(17), 7791–7795.
8 K. Yao, M. Zhai and Y. Ni, α-Ni $(OH)_2 \cdot 0.75\ H_2O$ nanofilms on Ni foam from simple $NiCl_2$ solution: Fast electrodeposition, formation mechanism and application as an efficient bifunctional electrocatalyst for overall water splitting in alkaline solution, *Electrochim. Acta*, 2019, **301**, 87–96.
9 B. Zhang, S. Xu, J. Li, *et al.*, Excellent electrocatalytic performance of $CuCo_2S_4$ nanowires for high-efficiency overall water splitting in alkaline and seawater media, *CrystEngComm*, 2025, **27**(22), 3700–3711.
10 W. Lu, T. Liu, L. Xie, C. Tang, D. Liu, S. Hao, F. Qu, G. Du, Y. Ma, A. M. Asiri and X. Sun, *In Situ* Derived Co–B Nanoarray: A High-Efficiency and Durable 3D Bifunctional Electrocatalyst for Overall Alkaline Water Splitting, *Small*, 2017, **13**, 1700805.
11 J. Xu, Y. Liu, J. Li, I. Amorim, B. Zhang, D. Xiong, N. Zhang, S. M. Thalluri, J. P. S. Sousa and L. Liu, Hollow cobalt phosphide octahedral pre-catalysts with exceptionally high intrinsic catalytic activity for electro-oxidation of water and methanol, *J. Mater. Chem. A*, 2018, **6**, 20646–20652.
12 Z. Xiao, Y. Wang, Y.-C. Huang, Z. Wei, C.-L. Dong, J. Ma, S. Shen, Y. Li and S. Wang, Filling the oxygen vacancies in Co_3O_4 with phosphorus: an ultra-efficient electrocatalyst for overall water splitting, *Energy Environ. Sci.*, 2017, **10**, 2563–2569.
13 S. Zhang, R. Y. Li, X. Li, *et al.*, Hydrothermally synthesized $NiSe_2$ nanospheres for efficient bifunctional electrocatalysis in alkaline seawater electrolysis: High performance and stability in HER and OER, *Mater. Res. Bull.*, 2025, **189**, 113463.
14 W. Zhang, Y. Sun, Q. Liu, J. Guo and X. Zhang, Vanadium and nitrogen co-doped CoP nanoleaf array as pH-universal electrocatalyst for efficient hydrogen evolution, *J. Alloys Compd.*, 2019, **791**, 1070–1078.
15 H. Zhou, Z. Zhang, Q. Zhang, *et al.*, Multidimensional Engineering Strategies for Transition Metal Selenide Electrocatalysts in Water Electrolysis with Performance Optimization Mechanisms and Future Perspectives, *Chem. Rec.*, 2025, 2500082.
16 W. Li, X. Gao, D. Xiong, F. Xia, J. Liu, W.-G. Song, J. Xu, S. M. Thalluri, M. F. Cerqueira, X. Fu and L. Liu, Vapor–solid synthesis of monolithic single-crystalline CoP nanowire electrodes for efficient and robust water electrolysis, *Chem. Sci.*, 2017, **8**, 2952–2958.
17 W. Zhu, W. Hu, Y. Wei, Y. Zhang, K. Pan, S. Zhang, X. Hang, M. Zheng and H. Pang, *Adv. Funct. Mater.*, 2024, **34**, 2409390.
18 H. J. Qiu, Y. Ito, W. Cong, Y. Tan, P. Liu, A. Hirata, T. Fujita, Z. Tang and M. Chen, Nanoporous Graphene with Single-Atom Nickel Dopants: An Efficient and Stable Catalyst for Electrochemical Hydrogen Production, *Angew. Chem., Int. Ed.*, 2015, **54**(47), 14031–14035.
19 T. Tang, W. J. Jiang, S. Niu, N. Liu, H. Luo, Y. Y. Chen, S. F. Jin, F. Gao, L. J. Wan and J. S. Hu, Electronic and Morphological Dual Modulation of Cobalt Carbonate Hydroxides by Mn Doping toward Highly Efficient and Stable Bifunctional Electrocatalysts for Overall Water Splitting, *J. Am. Chem. Soc.*, 2017, **139**(24), 8320–8328.
20 B. Zhang, Y. Zhao, X. Li, *et al.*, Rapidly reconstructed $CuCo_2S_4$@Co–V–O–F nanocatalysts for efficient and stable overall water splitting in alkaline and seawater electrolysis, *RSC Adv.*, 2025, **15**(24), 19443–19455.
21 S. Anantharaj, H. Sugime and S. Noda, Why shouldn't double-layer capacitance (C_{dl}) be always trusted to justify Faradaic electrocatalytic activity differences, *J. Electroanal. Chem.*, 2021, **903**, 115842.
22 Y. Zuo, D. Rao, S. Ma, T. Li, Y. H. Tsang, S. Kment and Y. Chai, Valence Engineering *via* Dual-Cation and Boron Doping in Pyrite Selenide for Highly Efficient Oxygen Evolution, *ACS Nano*, 2019, **13**(10), 11469–11476.
23 S. Anantharaj, S. Kundu and S. Noda, "The Fe Effect":A review unveiling the critical roles of Fe in enhancing OER activity of Ni and Co based catalysts, *Nano Energy*, 2021, **80**, 105514.
24 H. Yu, Y. Ma, Y. Pan, *et al.*, CoFe phosphide conversion to heterojunction metal phosphide (CoFeP) electrocatalysts for water splitting, *J. Mater. Sci. Eng. B*, 2024, **308**, 117589.
25 K. Fan, H. Chen, Y. Ji, *et al.*, Nickel–vanadium monolayer double hydroxide for efficient electrochemical water oxidation, *Nat. Commun.*, 2016, **7**(1), 11981.
26 X. Peng, L. Hu, L. Wang, *et al.*, Vanadium carbide nanoparticles encapsulated in graphitic carbon network nanosheets: a high-efficiency electrocatalyst for hydrogen evolution reaction, *Nano Energy*, 2016, **26**, 603–609.
27 H. Shi, H. Liang, F. Ming, *et al.*, Efficient overall water-splitting electrocatalysis using lepidocrocite VOOH hollow nanospheres, *Angew. Chem., Int. Ed.*, 2017, **56**, 573–577.
28 M. Xing, L. B. Kong, M. C. Liu, *et al.*, Cobalt vanadate as highly active, stable, noble metal-free oxygen evolution electrocatalyst, *J. Mater. Chem. A*, 2014, **2**, 18435–18443.
29 J. Zhang, B. Yuan, S. Cui, *et al.*, Facile synthesis of 3D porous Co_3- V_2O_8 nanoroses and 2D $NiCo_2V_2O_8$ nanoplates for high perfor- mance supercapacitors and their electrocatalytic oxygen evolution reaction properties, *Dalton Trans.*, 2017, **46**, 3295–3302.

30 L. Liardet and X. Hu, Amorphous cobalt vanadium oxide as a highly active electrocatalyst for oxygen evolution, *ACS Catal.*, 2018, **8**, 644–650.
31 D. Li, B. Zhang, Y. Li, *et al.*, Boosting hydrogen evolution activity in alkaline media with dispersed ruthenium clusters in NiCo-layered double hydroxide, *Electrochem. Commun.*, 2019, **101**, 23–27.
32 D. Li, B. Zhang, Y. Li, *et al.*, Boosting hydrogen evolution activity in alkaline media with dispersed ruthenium clusters in NiCo-layered double hydroxide, *Electrochem. Commun.*, 2019, **101**, 23–27.
33 S. Li, R. Ma, Y. Pei, *et al.*, Geometric structure and electronic polarization synergistically boost hydrogen evolution kinetics in alkaline medium, *J. Phys. Chem. Lett.*, 2020, **11**(9), 3436–3442.
34 G. Chen, T. Wang, J. Zhang, *et al.*, Accelerated hydrogen evolution kinetics on NiFe-layered double hydroxide electrocatalysts by tailoring water dissociation active sites, *Adv. Mater.*, 2018, **30**(10), 1706279.
35 Y. Feng, X. Wang and J. Wang, A nitridation route to construct high-activity interfaces toward alkaline hydrogen evolution, *J. Mater. Chem. A*, 2022, **10**(20), 11205–11212.
36 Y. Chen, G. Meng, Z. Chang, *et al.*, Construction of CoP_2-Mo_4P_3/NF heterogeneous interfacial electrocatalyst for boosting water splitting, *Nanomaterials*, 2022, **13**(1), 74.
37 H. Wei, A. Tan, W. Liu, *et al.*, Interface engineering-induced 1T-MoS_2/NiS heterostructure for efficient hydrogen evolution reaction, *Catalysts*, 2022, **12**(9), 947.
38 Y. Wei, J. Wang, Y. Shang, *et al.*, Fabrication of superaerophobic Ru-doped c-$CoSe_2$ for efficient hydrogen production, *J. Mater. Chem. A*, 2024, **12**(9), 5294–5306.
39 J. X. Guo, D. Y. Yan, K. W. Qiu, *et al.*, High electrocatalytic hydrogen evolution activity on a coupled Ru and CoO hybrid electrocatalyst, *J. Energy Chem.*, 2019, **37**, 143–147.
40 J. Liu, Y. Ji, J. Nai, *et al.*, Ultrathin amorphous cobalt–vanadium hydr (oxy) oxide catalysts for the oxygen evolution reaction, *Energy Environ. Sci.*, 2018, **11**(7), 1736–1741.
41 X. Ma, Q. Guo, J. Zhang, *et al.*, $[CH_3NH_3][M(HCOO)_3]$-based 2D porous $NiCo_2S_4$ nanosheets for high-performance supercapacitors with high power densities, *Chem. Eng. J.*, 2022, **437**, 135337.
42 P. Sun, Y. Zhou, H. Li, *et al.*, Round-the-clock bifunctional honeycomb-like nitrogen-doped carbon-decorated Co_2P/Mo_2C-heterojunction electrocatalyst for direct water splitting with 18.1% STH efficiency, *Appl. Catal., B*, 2022, **310**, 121354.
43 Y. Suchorski, L. Rihko-Struckmann, F. Klose, Y. Ye, M. Alandjiyska, K. Sundmacher and H. Weiss, Evolution of oxidation states in vanadium-based catalysts under conventional XPS conditions, *Appl. Surf. Sci.*, 2005, **249**, 231–237.
44 D. P. Zhao, M. Z. Dai, Y. Zhao, *et al.*, Improving electrocatalytic activities of FeCo2O4@ FeCo2S4@PPy electrodes by surface/interface regulation, *Nano Energy*, 2020, **72**, 104715.
45 W. Xi, G. Yan, H. Tan, *et al.*, Superaerophobic P-doped $Ni(OH)_2$/$NiMoO_4$ hierarchical nanosheet arrays grown on Ni foam for electrocatalytic overall water splitting, *Dalton Trans.*, 2018, **47**(26), 8787–8793.
46 K. Obata and K. Takanabe, A permselective CeOx coating to improve the stability of oxygen evolution electrocatalysts, *Angew. Chem.*, 2018, **130**(6), 1236–1632.
47 J. Su, Y. G. Yang, *et al.*, Ruthenium-cobalt nanoalloys encapsulated in nitrogen-doped graphene as active electrocatalysts for producing hydrogen in alkaline media, *Nat. Commun.*, 2017, **8**(1), 14969.
48 L. Y. Wang, W. J. Huan, F. Y. Jia, L. J. Lu, J. W. Zhu, P. Zhu, X. S. Zhao, G. X. Wang and S. Liu, Tailored crafting of CoP/Ni_2P nanoparticles coupled with N-Doped nanoporous carbon to enable efficient hydrogen and oxygen evolution, *Energy Fuels*, 2022, **36**, 12245–12252.
49 B. Li, Z. Li, Q. Pang and J. Z. Zhang, Core/shell cable-like Ni_3S_2 nanowires/N-doped graphene-like carbon layers as composite electrocatalyst for overall electrocatalytic water splitting, *Chem. Eng. J.*, 2020, **401**(126045).
50 L. Guo, J. Chi, T. Cui, *et al.*, Phosphorus Defect Mediated Electron Redistribution to Boost Anion Exchange Membrane-Based Alkaline Seawater Electrolysis, *Adv. Energy Mater.*, 2024, **14**(31), 2400975.
51 A. Talebi and G. B. Darband, Ultra-fast one-step electrochemical synthesize of Ni-Mn-P as an active and stable electrocatalyst for green hydrogen production, *Fuel*, 2025, **397**, 135427.
52 E. Allahyari, G. B. Darband and A. Davoodi, A novel surface engineering approach for the synthesis of Ni–Mn–P@ Co–S nanosheets as an advanced electrocatalyst for hydrogen evolution reaction, *Int. J. Hydrogen Energy*, 2025, **116**, 115–127.
53 X. Huo, G. Shan, L. Yang, *et al.*, Insights into kinetic and transfer mechanisms for alkaline decoupled water electrolysis based on distribution of relaxation times, *Int. J. Hydrogen Energy*, 2024, **91**, 693–702.
54 J. Zuo, N. Y. Steiner, Z. Li, *et al.*, Quantitative investigation of internal polarization in a proton exchange membrane water electrolyzer stack using distribution of relaxation times, *Appl. Energy*, 2025, **386**, 125543.
55 L. Lukashuk, N. Yigit, R. Rameshan, *et al.*, Operando insights into CO oxidation on cobalt oxide catalysts by NAP-XPS, FTIR, and XRD, *ACS Catal.*, 2018, **8**(9), 8630–8641.
56 M. Du, Z. Miao, H. Li, *et al.*, Oxygen-vacancy and phosphate coordination triggered strain engineering of vanadium oxide for high-performance aqueous zinc ion storage, *Nano Energy*, 2021, **89**, 106477.
57 J. Liang, Z. Li, X. He, Y. Luo, D. Zheng, Y. Wang, T. Li, B. Ying, S. Sun, Z. Cai, Q. Liu and B. Tang, *Mater. Today*, 2023, **69**, 193–235.
58 Y. Pan, F. Zhao, G. Ji, *et al.*, Electrocatalytic performance of Ni-based high-entropy alloys with unique structural features in alkaline and seawater electrolysis under −10 °C, *Int. J. Hydrogen Energy*, 2025, **127**, 147–159.

59 J. Guo, Y. Zheng, Z. Hu, *et al.*, Direct seawater electrolysis by adjusting the local reaction environment of a catalyst, *Nat. Energy*, 2023, **8**(3), 264–272.
60 R. Abedi and G. B. Darband, Interfacial surface engineering of Co-Mn-P ultrathin nanosheets on Ni-Co hierarchical nanostructure for boosting electrochemical active sites in overall water splitting, *J. Power Sources*, 2025, **641**, 236840.
61 Y. Cheng, X. Guo, Z. Ma, *et al.*, Highly Efficient and Stable Mn-Co1. 29Ni1. 71O4 Electrocatalysts for Alkaline Water Electrolysis: Atomic Do Strategy for Enhanced OER and HER Performance, *Molecules*, 2025, **30**(5), 1162.
62 H. Hu, Z. Zhang, L. Liu, *et al.*, Efficient and durable seawater electrolysis with a V2O3-protected catalyst, *Sci. Adv.*, 2024, **10**(20), eadn7012.
63 J. Kim, J. H. Seo, J. K. Lee, *et al.*, Challenges and strategies in catalysts design towards efficient and durable alkaline seawater electrolysis for green hydrogen production, *Energy Mater.*, 2025, **5**(500076).
64 M. A. Ehsan, *et al.*, Direct deposition of amorphous cobalt–vanadium mixed oxide films for electrocatalytic water oxidation, *ACS Omega*, 2019, **4**(7), 12671–12679, DOI: **10.1021/acsomega.9b01385**.
65 D. Liu, H. Xu, C. Wang, H. Shang, R. Yu, Y. Wang, J. Li, X. Li and Y. Du, 3D Porous Ru-Doped NiCo-MOF Hollow Nanospheres for Boosting Oxygen Evolution Reaction Electrocatalysis, *Inorg. Chem.*, 2021, **60**(8), 5882–5889.
66 K. Zhang, W. Ma, G. Tan, *et al.*, Interfacial engineering of Ru-doped Co_3O_4/CoP nanowires heterostructure as efficient bifunctional electrocatalysts for alkaline water splitting, *Mol. Catal.*, 2022, **530**, 112640.
67 Y. Yang, Q. Liu, H. Wang, *et al.*, Phosphorus-doped 3D RuCo nanowire arrays on nickel foam with enhanced electrocatalytic activity for overall water splitting, *ACS omega*, 2021, **6**(15), 10234–10241.
68 T. Wang, X. Zhang, X. Yu, *et al.*, Interfacial interaction in NiFe LDH/NiS_2/VS_2 for enhanced electrocatalytic water splitting, *Molecules*, 2024, **29**(5), 951.
69 W. Li, B. Feng, L. Yi, *et al.*, Highly efficient alkaline water splitting with Ru-doped Co–V layered double hydroxide nanosheets as a bifunctional electrocatalyst, *ChemSusChem*, 2021, **14**(2), 730–737.